

Deep reinforcement learning for smart calibration of radio telescopes

Sarod Yatawatta¹[★] and Ian M. Avruch[†]

¹*ASTRON, Oude Hoogeveensedijk 4, 7991 PD Dwingeloo, The Netherlands*

1 April 2022

ABSTRACT

Modern radio telescopes produce unprecedented amounts of data, which are passed through many processing pipelines before the delivery of scientific results. Hyperparameters of these pipelines need to be tuned by hand to produce optimal results. Because many thousands of observations are taken during a lifetime of a telescope and because each observation will have its unique settings, the fine tuning of pipelines is a tedious task. In order to automate this process of hyperparameter selection in data calibration pipelines, we introduce the use of reinforcement learning. We test two reinforcement learning techniques, twin delayed deep deterministic policy gradient (TD3) and soft actor-critic (SAC), to train an autonomous agent to perform this fine tuning. For the sake of generalization, we consider the pipeline to be a black-box system where the summarized state of the performance of the pipeline is used by the autonomous agent. The autonomous agent trained in this manner is able to determine optimal settings for diverse observations and is therefore able to perform *smart* calibration, minimizing the need for human intervention.

Key words: Instrumentation: interferometers; Methods: numerical; Techniques: interferometric

1 INTRODUCTION

Data processing pipelines play a crucial role for modern radio telescopes, where the incoming data flow is reduced in size by many orders of magnitude before science-ready data are produced. In order to achieve this, data are passed through many processing steps, for example, to mitigate radio frequency interference (RFI), to remove strong confusing sources and to correct for systematic errors. Calibration is one crucial step in these interferometric processing pipelines, not only to correct for systematic errors in the data, but also to subtract strong outlier sources such that weak RFI mitigation can be carried out. Most modern radio telescopes are general purpose instruments because they serve diverse science cases. Therefore, depending on the observational parameters such as the direction in the sky, observing frequency, observing time (day or night) etc., the processing pipelines need to be adjusted to realize the potential quality of the data.

The best parameter settings for each pipeline are mostly determined by experienced astronomers. This requirement for hand tuning is problematic for radio telescopes that stream data uninterruptedly. In this paper, we propose the use of autonomous agents to replace the human aspect in fine-tuning pipeline settings. We focus on calibration pipelines, in particular, distributed calibration pipelines where data at multiple frequencies are calibrated together, in a distributed computer (Yatawatta 2015; Brossard et al. 2016; Yatawatta et al. 2018; Ollier et al. 2018; Yatawatta 2020). In this setting, the smoothness of systematic errors across frequency is exploited to get a better quality solution, as shown by results with real and simulated data (Patil et al. 2017; Mertens et al. 2020; Mevius et al. 2021). The quality can be further improved by enforcing spatial regularization

(Yatawatta 2020), which in turn adds more hyperparameters. A comparable situation exists in multispectral image synthesis pipelines as well (Ammanouil et al. 2019), where the determination of the optimal hyperparameters is computationally expensive.

One key hyperparameter that needs fine-tuning in a distributed calibration setting is the regularization factor for the smoothness of solutions across frequency. Note that spatial smoothness will increase the number of hyperparameters but the methods developed in this paper will be applicable in those cases as well. It is possible to select the regularization analytically (Yatawatta 2016), however, extending this to calibration along multiple directions is not optimal. This is because directions that are spread over a wide field of view will have highly uncorrelated systematic errors due to the antenna beam and ionosphere, thus requiring the fine-tuning of the regularization per each direction. In this paper, we train an autonomous agent to predict the regularization factors for a distributed, multi-directional calibration pipeline. The calibration pipeline will perform calibration with a cadence of a few seconds to a few minutes of data. Therefore, for an observation of long duration the calibration pipeline needs to be run many times. At the beginning of every observation the autonomous agent will recommend the regularization factors to be used in the pipeline based on the pipeline *state* and will update the regularization factors at the required cadence. This concept can be extended to train autonomous agents that do more than hyperparameter tuning, for example to optimally allocate compute resources.

We train the autonomous agent using reinforcement learning (RL) (Sutton & Barto 2018). Reinforcement learning is a branch of machine learning where an agent is trained by repeated interactions with its environment, with proper rewards (or penalties) awarded whenever a correct (or incorrect) decision (or action) is made. In our case, the environment or the observations made by the agent are: i) the input data to the pipeline ii) the input sky model to the pipeline used

[★] E-mail: yatawatta@astron.nl

[†] E-mail: ian.professional@avruch.net

in calibration iii) the output solutions, and, iv) the output residual data from the pipeline. In order to minimize the computational cost, we do not feed data directly to the agent. Instead, we only feed the minimum required information of the performance of the pipeline (also called the *state*) to the agent. Because the calibration is done with a small time-frequency interval, the amount of data used to determine the state is also small (compared with the full observation). The determination of the reward is done considering two factors. First, the calibration should perform accurately such that the variance of the residual data should be lower than the input data (scaled by the correction applied during calibration). Secondly, we should not overfit the data, which will suppress signals of scientific interest in the residual. Unlike supervised learning, we do not have access to ground-truth information to determine this overfitting. Instead, in order to measure the overfitting, we use the influence function (Hampel et al. 1986; Cook & Weisberg 1982; Koh & Liang 2017). The influence function is useful for assessing a statistical estimator's robustness against errant data.

The influence function can be formally described as follows (Hampel et al. 1986): Consider a vector statistic \mathbf{T} which operates on the data vector \mathbf{x} . The cumulative density function (cdf) of the random process with \mathbf{x} samples is \mathcal{F} . The statistic \mathbf{T} is a composition of operations on the data (a simple example is the mean of the data). The statistic \mathbf{T} is related to the statistical functional \mathcal{T} as $\mathbf{T} = \mathcal{T}(\hat{\mathcal{F}})$ where $\hat{\mathcal{F}}$ is the empirical cdf (note that the statistical functional operates on the cdf while the statistic operates on the data). With this setting, we define the influence function $IF_{\mathcal{T}, \mathcal{F}}(\mathbf{x})$ as

$$IF_{\mathcal{T}, \mathcal{F}}(\mathbf{x}) = \lim_{\epsilon \rightarrow 0} \frac{\mathcal{T}((1 - \epsilon)\mathcal{F} + \epsilon\delta_{\mathbf{x}}) - \mathcal{T}(\mathcal{F})}{\epsilon}$$

where $\delta_{\mathbf{x}}$ is a unit point mass probability¹ located at \mathbf{x} . The influence function is a generalization of the derivative for statistical functionals, and can be seen as the sensitivity of \mathcal{T} to a change in the cdf \mathcal{F} due to an additional datum. By studying $IF_{\mathcal{T}, \mathcal{F}}(\mathbf{x})$, we can study the behavior of \mathcal{T} to perturbations of data and consequently, we can study the behavior of \mathbf{T} to perturbations of data.

In this paper, we consider the residual of the data after calibration as the statistic \mathbf{T} . We are interested in studying the effect of model incompleteness on the output residual. One operation in calibration is a minimization (or an $\arg \min(\cdot)$) and the derivation of the influence function for this case is more involved. We have derived this in our previous work (Yatawatta 2018, 2019). We build on this result and determine the reward by considering both the noise reduction and the influence function of calibration. To summarize, we consider both the bias and the variance (Geman et al. 1992) introduced by the pipeline for the determination of the state as well as the reward. The agent will perform an action, that is to recommend the optimal regularization factors to use in the calibration pipeline. Compared to conventional methods of hyperparameter fine-tuning (Bergstra & Bengio 2012; Bates et al. 2021), the agent will make a decision much faster, but on the other hand, the training of the agent will incur additional initial cost.

The advent of deep neural networks (deep learning) (LeCun et al. 2015) combined with better training algorithms have enabled RL agents to perform superhuman tasks. Early RL breakthroughs were made in discrete action spaces such as in computer games (Mnih et al. 2015). The regularization factors used in calibration are in a continuous action space, and therefore, in this paper we use RL

techniques suitable for continuous action spaces, namely, deep deterministic policy gradient (DDPG) (Lillicrap et al. 2015) and its improvements, TD3 (Fujimoto et al. 2018) and SAC (Haarnoja et al. 2018). In this paper, we only consider calibration pipelines that perform distributed, direction dependent calibration, but the same RL technique can be used in other data processing pipelines in radio astronomy and beyond.

The rest of the paper is organized as follows. In section 2, we describe the distributed, direction dependent calibration pipeline. In section 3, we introduce our RL agent and its environment. In section 4, we provide results based on simulated data to show the efficacy of the trained RL agent. Finally, we draw our conclusions in section 5.

Notation: Lower case bold letters refer to column vectors (e.g. \mathbf{y}). Upper case bold letters refer to matrices (e.g. \mathbf{C}). Unless otherwise stated, all parameters are complex numbers. The set of complex numbers is given as \mathbb{C} and the set of real numbers as \mathbb{R} . The matrix inverse, pseudo-inverse, transpose, Hermitian transpose, and conjugation are referred to as $(\cdot)^{-1}$, $(\cdot)^{\dagger}$, $(\cdot)^T$, $(\cdot)^H$, $(\cdot)^*$, respectively. The matrix Kronecker product is given by \otimes . The vectorized representation of a matrix is given by $\text{vec}(\cdot)$. The identity matrix of size N is given by \mathbf{I}_N . All logarithms are to the base e , unless stated otherwise. The Frobenius norm is given by $\|\cdot\|$ and the L1 norm is given by $\|\cdot\|_1$.

2 DISTRIBUTED DIRECTION DEPENDENT CALIBRATION PIPELINE

In this section, we first give a brief overview of the distributed, direction dependent calibration pipeline that is used by the RL agent for hyperparameter tuning. Thereafter, we give an overview of performance analysis of the calibration pipeline using influence functions.

2.1 Distributed calibration

We refer the reader to Yatawatta (2015); Yatawatta (2020) for an in-depth overview of distributed calibration. We outline the basic concepts here.

The signal (in full polarization) received by an interferometer is given by (Hamaker et al. 1996)

$$\mathbf{V}_{pqf} = \sum_{k=1}^K \mathbf{J}_{kpf} \mathbf{C}_{kpqf} \mathbf{J}_{kqf}^H + \mathbf{N}_{pqf} \quad (1)$$

where we have signals from K discrete sources in the sky being received. All items in (1), i.e., \mathbf{V}_{pqf} , \mathbf{C}_{kpqf} , \mathbf{J}_{kpf} , \mathbf{J}_{kqf} , $\mathbf{N}_{pqf} \in \mathbb{C}^{2 \times 2}$ are implicitly time varying and subscripts p, q correspond to stations p and q , f correspond to the receiving frequency, and k correspond to the source index. The coherency of the k -th source at baseline p - q is given by \mathbf{C}_{kpqf} and for a known source, this can be pre-computed (Thompson et al. 2001). The noise \mathbf{N}_{pqf} consists of the actual thermal noise as well as signals from sources in the sky that are not part of the model. The systematic errors due to the propagation path (ionosphere), receiver beam, and receiver electronics are represented by \mathbf{J}_{kpf} and \mathbf{J}_{kqf} . For each time and frequency, with N stations, we have $N(N-1)/2$ pairs of p - q .

Calibration is the estimation of \mathbf{J}_{kpf} for all k, p and f , using data within a small time interval (say Δ_t), within which it is assumed that \mathbf{J}_{kpf} remains constant. An important distinction is that we only calibrate along K directions, but in real observations, there are signals from faint sources (including the Galaxy) that are not being modeled. We are not presenting a method of calibration in this paper, and therefore the actual method of calibration is not relevant. However,

¹ $\delta_{\mathbf{x}}$ operates in cdf space, similar to a Heaviside step function.

for the sake of simplicity, we follow a straightforward description. What we intend to achieve is to relate the hyperparameters used in the pipeline to the performance of calibration. Therefore, we represent $\mathbf{J}_{kp f} \in \mathbb{C}^{2 \times 2}$ as 8 real parameters (for frequency f and direction k), and we have $8 \times N \times K$ real parameters in total for frequency f , per direction, namely θ_{kf} .

We represent the matrix equation (1) in vector form as

$$\mathbf{v}_{pqf} = \sum_{k=1}^K \mathbf{s}_{kpqf}(\theta_{kf}) + \mathbf{n}_{pqf} \quad (2)$$

where $\mathbf{s}_{kpqf}(\theta_{kf}) = (\mathbf{J}_{kp f}^* \otimes \mathbf{J}_{kp f}) \text{vec}(\mathbf{C}_{kpqf})$, $\mathbf{v}_{pqf} = \text{vec}(\mathbf{V}_{pqf})$, and $\mathbf{n}_{pqf} = \text{vec}(\mathbf{N}_{pqf})$.

We stack up the data and model vectors of (2) for the Δ_t time slots within which a single solution is obtained as

$$\begin{aligned} \mathbf{x}_f &= [\text{real}(\mathbf{v}_{12}^T), \text{imag}(\mathbf{v}_{12}^T), \text{real}(\mathbf{v}_{13}^T), \dots]^T \\ \mathbf{s}_{kf}(\theta_{kf}) &= [\text{real}(\mathbf{s}_{k12f}(\theta)^T), \text{imag}(\mathbf{s}_{k12f}(\theta)^T), \text{real}(\mathbf{s}_{k13f}(\theta)^T), \\ &\quad \dots]^T \end{aligned}$$

which are vectors of size $8 \times N(N-1)/2 \times \Delta_t$ and we have

$$\mathbf{x}_f = \sum_{k=1}^K \mathbf{s}_{kf}(\theta_{kf}) + \mathbf{n}_f = \mathbf{s}_f(\theta_f) + \mathbf{n}_f \quad (4)$$

as our final measurement equation with real valued vectors $\theta_{kf} \in \mathbb{R}^{8N}$, $\theta_f \in \mathbb{R}^{8KN}$.

In order to estimate θ_{kf} from (4), we define a loss function

$$g_{kf}(\theta_{kf}) = \text{loss}(\mathbf{x}_f, \theta_{kf}) \quad (5)$$

depending on the noise model, for example, mean squared error loss, $\|\mathbf{x}_f - \mathbf{s}_f(\theta_f)\|^2$. We calibrate data at many frequencies and we exploit the smoothness of θ_{kf} with f and in order to make the solutions smooth. We introduce the constraint

$$\theta_{kf} = \mathbf{Z}_k \mathbf{b}_f \quad (6)$$

where $\mathbf{b}_f \in \mathbb{R}^P$ is a polynomial basis vector in frequency (P terms) evaluated at f and $\mathbf{Z}_k \in \mathbb{R}^{8N \times P}$ is a matrix that shares information about the contribution of each basis function over all frequencies. In addition, we can introduce constraints for spatial smoothness (using B bases in space) as

$$\mathbf{Z}_k = \bar{\mathbf{Z}}_k = \mathbf{Z} \mathbf{B}_k \quad (7)$$

where \mathbf{B}_k is a basis matrix ($\in \mathbb{R}^{B \times P}$) evaluated along the direction k and $\mathbf{Z} \in \mathbb{R}^{8N \times B}$ is a matrix that shares information common to all K directions in the sky.

We introduce Lagrange multipliers $\mathbf{w}_{kf} \in \mathbb{R}^{8N}$ for the constraint (6) and $\mathbf{W}_k \in \mathbb{R}^{8N \times P}$ for the constraint (7). We use the augmented Lagrangian method (or method of multipliers) (Hestenes 1969; Powell 1969) to solve this. We write the augmented Lagrangian as

$$\begin{aligned} l(\theta_{kf}, \mathbf{w}_{kf}, \mathbf{W}_k, \mathbf{Z}_k, \mathbf{Z} : \forall k, f) = \\ \sum_{kf} g_{kf}(\theta_{kf}) + \mathbf{w}_{kf}^T (\theta_{kf} - \mathbf{Z}_k \mathbf{b}_f) + \frac{\rho_k}{2} \|\theta_{kf} - \mathbf{Z}_k \mathbf{b}_f\|^2 \\ + \sum_k \mathbf{W}_k^T (\mathbf{Z}_k - \bar{\mathbf{Z}}_k) + \frac{\alpha_k}{2} \|\mathbf{Z}_k - \bar{\mathbf{Z}}_k\|^2 \end{aligned} \quad (8)$$

which we minimize to find a smooth solution. As described in (Yatawatta 2020), we use a combination of alternating direction method of multipliers (Boyd et al. 2011) and (weighted) federated averaging (McMahan et al. 2016) to solve this.

The hyperparameters in (8) are the regularization factors $\alpha_k, \rho_k \in \mathbb{R}^+$, where we have two regularization factors per each direction k . However, for the remainder of the paper, for simplicity, we only consider the constraint (6) and ignore the constraint (7). Therefore, we need to select K positive, real valued hyperparameters to get the optimal solution to (8). We can consider the K directional calibration as K separate sub problems and find analytical solutions to optimal ρ_k as done in Yatawatta (2016). However, by considering each direction separately, we ignore the inter-dependencies between directions, thereby making our optimal ρ_k only an approximation. If we consider the constraint (7) as well, the complexity of selecting the optimal α_k, ρ_k increases. The alternative is to use handcrafted methods such as grid search but this is infeasible, as every observation will have unique requirements for grid search hyperparameters. In section 3, we will present the use of RL to automatically find the best values for ρ_k considering all K directions together (which can be extended to find α_k as well).

2.2 Performance analysis using the influence function

The RL agent interacts with the pipeline (the pipeline is solving (8), see Fig. 2) to recommend the best values for ρ_k . In order to do this, the RL agent needs to have some information about the environment (i.e., the performance of the pipeline). The performance is measured using the influence function (see section 1) of the output statistic, i.e., the residual. After each calibration, we calculate the residual using (1) as

$$\mathbf{R}_{pqf} = \mathbf{V}_{pqf} - \sum_{k=1}^K \hat{\mathbf{J}}_{kp f} \mathbf{C}_{kpqf} \hat{\mathbf{J}}_{kp f}^H \quad (9)$$

where $\hat{\mathbf{J}}_{kp f} \forall k, p, f$ are calculated using the solutions obtained for θ_{kf} .

In order to analyze the influence function of the residual, we reformulate our data model using real vectors. We can rewrite (4) in a simplified form (dropping the subscripts k, f) as

$$\mathbf{x} = \mathbf{s}(\theta) + \mathbf{n} \quad (10)$$

where $\mathbf{x} \in \mathbb{R}^D$ is the data ($D = 8 \times N(N-1)/2 \times \Delta_t$), $\mathbf{s}(\theta)$ is our model and \mathbf{n} is the noise (noise as defined in (1) which includes unmodeled sources in the field of view). We find a solution to θ by minimizing a loss $g(\theta)$, say $\hat{\theta} = \arg \min_{\theta} g(\theta)$. Thence, we calculate the residual as

$$\mathbf{y} = \mathbf{x} - \mathbf{s}(\hat{\theta}). \quad (11)$$

To recapitulate, \mathbf{x} in (11) is the vectorized version of \mathbf{V}_{pqf} in (9) and \mathbf{y} is the vectorized version of \mathbf{R}_{pqf} , for all p, q within Δ_t (real and imaginary parts separate). Referring back to our definition of influence function in section 1, we consider the residual \mathbf{y} to be a statistic that is derived from the data \mathbf{x} . We have shown (Yatawatta 2019) that the probability density functions (pdf) of \mathbf{x} and \mathbf{y} , i.e., $p_X(\mathbf{x})$, $p_Y(\mathbf{y})$ are related as

$$p_X(\mathbf{x}) = |\mathcal{J}| p_Y(\mathbf{y}) \quad (12)$$

where $|\mathcal{J}|$ is the Jacobian determinant of the mapping from \mathbf{x} to \mathbf{y} . We can use (12) to find the mapping between the cumulative density functions and relate it to the formal definition of $IF_{\mathcal{T}, \mathcal{F}}(\mathbf{x})$ in section 1, but for our purpose, working with the pdf relation (12) is sufficient. Using (11), we can show that

$$|\mathcal{J}| = \exp \left(\sum_{i=1}^D \log(1 + \lambda_i(\mathcal{A})) \right) \quad (13)$$

where

$$\mathcal{A} = \frac{\partial \mathbf{s}(\boldsymbol{\theta})}{\partial \boldsymbol{\theta}^T} \left(\frac{\partial^2 \mathbf{g}(\boldsymbol{\theta})}{\partial \boldsymbol{\theta} \partial \boldsymbol{\theta}^T} \right)^{-1} \frac{\partial^2 \mathbf{g}(\boldsymbol{\theta})}{\partial \boldsymbol{\theta} \partial \mathbf{x}^T} \quad (14)$$

evaluated at $\boldsymbol{\theta} = \hat{\boldsymbol{\theta}}$. Ideally, we should have $|\mathcal{J}| = 1$ and therefore all eigenvalues of \mathcal{A} , $\lambda_i(\mathcal{A}) = 0$. But in practice, due to model error and degeneracies in the model, we have some non-zero values for $\lambda_i(\mathcal{A})$.

Let us denote the n -th element of \mathbf{x} in (11) as x_n . As \mathbf{x} is simply a reorganization of $\mathbf{V}_{p'q'f}$ in (9), given any value of $n \in [0, D-1]$, we can find the corresponding baseline $p' - q'$ as well as the corresponding element in the matrix $\mathbf{V}_{p'q'f}$ and whether it represents the real or imaginary part of that element. Let us use $l \in [0, 7]$, 4 complex correlation values) to denote this index in the matrix $\mathbf{V}_{p'q'f}$. Note that for the same baseline $p' - q'$ and l , we will have Δ_t values in the vector \mathbf{x} because we use multiple time ordered samples from the same baseline. Nonetheless, given n , we can find the corresponding $p' - q'$ and l and vice versa. Therefore, we use the notation x_n and $x_{p'q'l}$ to denote the same element in the vector \mathbf{x} . A similar relation exists between the n -th element of \mathbf{y} in (11) and the corresponding element of \mathbf{R}_{pqf} in (9).

Using (14), and using the dual notation described above, we can calculate $\frac{\partial \mathbf{y}}{\partial x_{p'q'l f}}$. Reordering the matching 8 values of $\frac{\partial \mathbf{y}}{\partial x_{p'q'l f}}$ as a matrix $\in \mathbb{C}^{2 \times 2}$, we can also find $\frac{\partial \mathbf{R}_{pqf}}{\partial x_{p'q'l f}}$. Finally, we find $E\{\frac{\partial \mathbf{R}_{pqf}}{\partial x_{p'q'l f}}\}$ where the expectation $E\{\cdot\}$ is taken over p', q' (excluding the tuple p, q) and $l \in [0, 7]$. Note that $E\{\frac{\partial \mathbf{R}_{pqf}}{\partial x_{p'q'l f}}\}$ has the same size as \mathbf{R}_{pqf} . Therefore, we can replace the residual \mathbf{R}_{pqf} with $E\{\frac{\partial \mathbf{R}_{pqf}}{\partial x_{p'q'l f}}\}$ when we produce the output and feed this to imaging, just like we make images of the residual. We call the image made in the usual radio astronomical image synthesis manner, replacing the residual \mathbf{R}_{pqf} with $D \times E\{\frac{\partial \mathbf{R}_{pqf}}{\partial x_{p'q'l f}}\}$, as the *influence map*, which we denote by $\mathcal{I}(\boldsymbol{\theta})$.

We illustrate the relationship between the (Stokes I) images made using the residual and its influence function in Fig. 1. We have simulated an observation (see section 4.2) with $K = 10$ directions in the sky being calibrated. The sky model has errors due to weak sources that are not being part of calibration. All images are centred at the phase centre, with size 128×128 pixels (pixel size $20'' \times 20''$), and are made using uniform imaging weights. An important fact is that the images are made using only 1 min of data (which is far less than the full observation). The left column (panels a and c) in Fig. 1 shows the residual while the right column (panels b and d) shows the influence map $\mathcal{I}(\boldsymbol{\theta})$. The top row is with low regularization (about 1/10 of the optimal value) and the bottom row is with approximately optimal regularization. Images of the residual show hardly any difference as seen in Fig. 1 (a) and (c). This is expected because we only use 1 min of data and the subtle differences due to imperfect calibration will only become apparent after processing more data (at least several hours). In contrast, the influence maps in Fig. 1 (b) and (d) clearly show a difference. Therefore, we conclude that by using $\mathcal{I}(\boldsymbol{\theta})$, with minimal amount of data, we are able to measure the performance of calibration. In section 3, we will discuss how to train deep neural networks to detect changes in the influence maps and evaluate the performance of calibration.

We relate the influence map to the bias and variance of calibration residual as follows. The bias is primarily caused by the errors in the sky model (difference between the true sky and the sky model used in calibration). If we consider the solutions to calibration, i.e. $\hat{\boldsymbol{\theta}}$, with low regularization we will have low bias and high variance

of the solutions (overfitting compared to the ground truth) and with high regularization, we will have high bias and low variance of the solutions (underfitting). We can reduce the bias by increasing the model complexity or by decreasing the regularization and conversely, we can reduce the variance by increasing the regularization. From Fig. 1 we see that low regularization leads to high influence and therefore the variance is directly related to the influence. We relate this result to the residual data \mathbf{y} in (11) as well. With high variance of $\hat{\boldsymbol{\theta}}$, the coherent information hidden in \mathbf{y} are affected with high variance. In other words, there is a loss of coherence and the coherent weak signals in \mathbf{y} get suppressed. The fine tuning of ρ_k will give us the optimal tradeoff between bias and the variance of the residual data. An example of this behavior is shown in Fig. 5. We achieve this fine-tuning using RL as described in section 3.

3 REINFORCEMENT LEARNING

In this section, we describe the basic concepts of reinforcement learning, especially tailored to our problem and thereafter we go into specific details about our RL agent. An RL agent interacts with its environment via some observations and performs an action depending on these observations and the current state of the agent. The objective of the agent is to maximize its reward depending on the action it performs. As shown in Fig. 2, our agent interacts with our calibration pipeline, which is the environment. We describe these interactions as follows:

- At an instance indexed by t , the input to the agent is given by state s_t (a real valued tensor). This is a summary of the observation that we deem sufficient for the agent to evaluate its action. In our case, we give the sky model used in calibration as part of s_t . In addition, we create an influence map $\mathcal{I}(\boldsymbol{\theta})$, that summarizes the performance of calibration as part of s_t . Note that we do not feed the data or the metadata (such as the uv coverage) into the agent. This way, our agent will be able to interact with pipelines operating at variable data rates and with variable solution intervals in calibration. The amount of data and the metadata are much larger than the size of s_t . Hence, the computational burden of the agent will also be reduced.
- Depending on s_t and its internal parameter values, the agent performs (or recommends) an action a_t (a real valued vector). In our case, the action is the specification of the regularization factors ρ_k (K values) which is fed back to the pipeline.
- We determine the reward r_t (a real valued scalar) to the agent using two criteria. First, we compare the noise of the input data σ_0 and the output residual σ_1 of the pipeline (by making images of the field being observed as in Fig. 1 left column or by time differencing the data) and find the ratio $\frac{\sigma_0}{\sigma_1}$. We get a higher reward as this ratio grows. Second, we look at the influence map and find its standard deviation, whose inverse we add to the reward. If we have high influence, we will get a smaller reward. With both these components constituting the reward, we aim to minimize both the bias and the variance of the pipeline.

Note that unlike in most RL scenarios, we do not have a terminal state (such as in a computer game where a player wins or loses). We terminate when we reach L iterations of refinement on ρ_k . The general interactions between the RL agent and the environment are given in Algorithm 1 and we make some remarks about Algorithm 1 here:

- The interactions shown in Algorithm 1 are for the learning or training phase of the RL agent. In this training phase, we simulate realistic observations (line 4) which we describe in section 4.2. The number of simulations (or episodes) is E .
- After the agent has been sufficiently trained, we can use it in

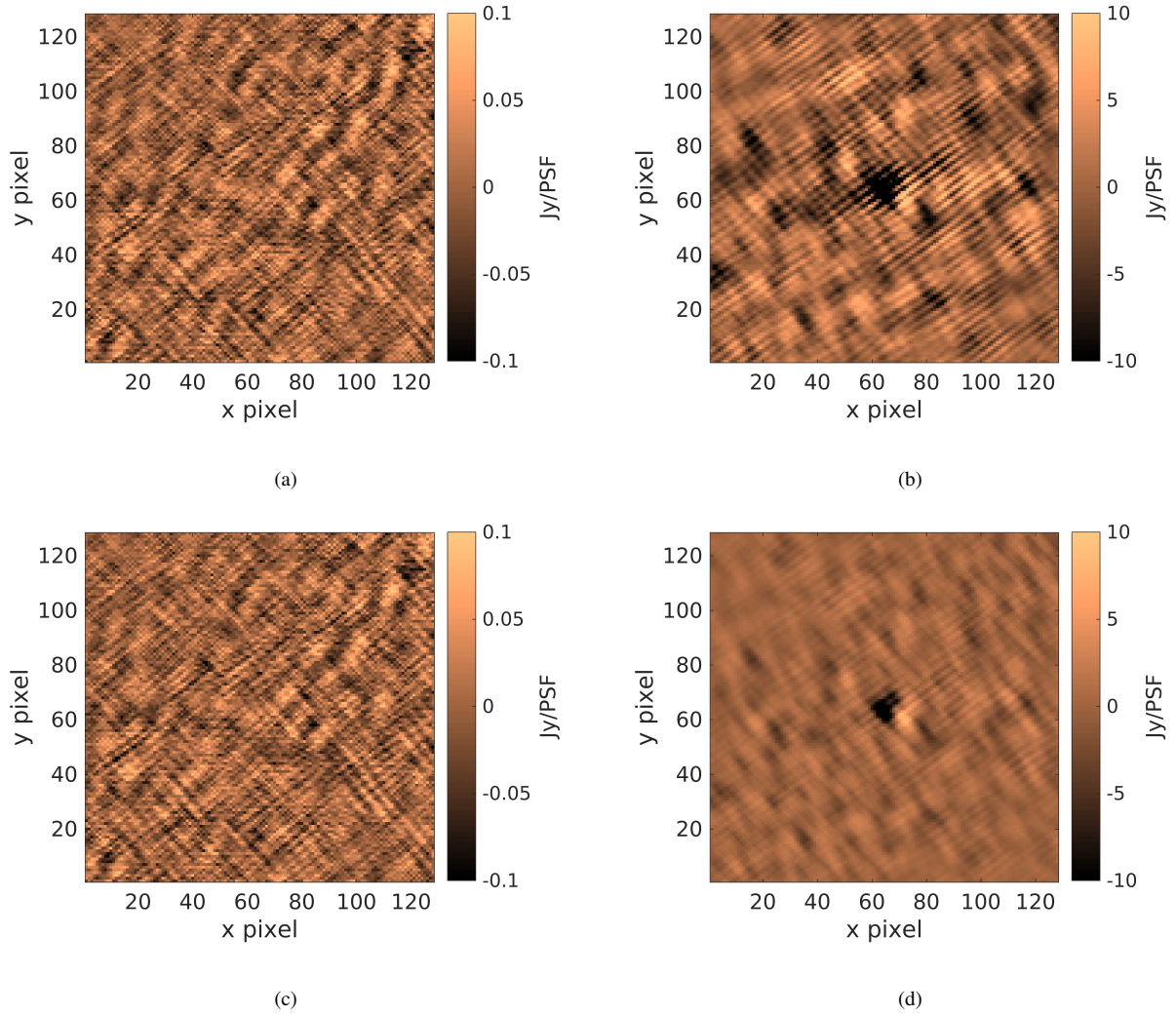


Figure 1. The residual and the corresponding influence maps for two calibration scenarios, using 1 min of data. The residual images are shown in panels (a) and (c) while the influence maps are shown in panels (b) and (d). The top row of panels are for calibration with low than optimal regularization while the bottom row panels are for optimal regularization.

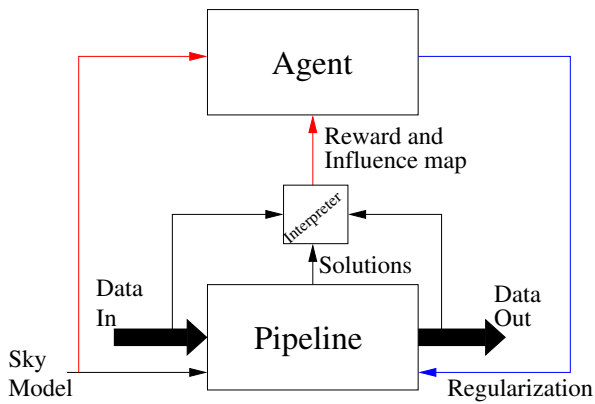


Figure 2. The interactions between the RL agent and its environment, i.e., the pipeline. The pipeline processes data in a stream and only a summarized state of the performance of the pipeline, calculated by the interpreter, is sent to the agent.

Algorithm 1 Training the RL agent

Require: Number of episodes E , Number of loop iterations L

- 1: Initialize Environment and Agent
- 2: Setup empty (or reload saved) ReplayBuffer
- 3: **for** $e = 1, \dots, E$ **do**
- 4: Environment: simulate new (random) observation
- 5: Agent: \leftarrow initial state s_0
- 6: **for** $t = 1, \dots, L$ **do**
- 7: { Agent starts interactions }
- 8: $a_t \leftarrow$ Agent suggests action based on s_t
- 9: Environment: take action a_t , determine reward r_t and next state s_{t+1}
- 10: ReplayBuffer: store (s_t, a_t, r_t, s_{t+1})
- 11: Agent: sample a mini-batch from ReplayBuffer and learn
- 12: **end for**
- 13: **end for**

processing real observations. In other words, we will have only one episode, $E = 1$ and line 4 of Algorithm 1 is replaced by the data from the observation. The learning step in line 11 is not necessary.

	TD3	SAC
Critic	$Q_{\xi_1}(s, a)$ and $Q_{\xi_2}(s, a)$ target $Q_{\bar{\xi}_1}(s, a)$ and $Q_{\bar{\xi}_2}(s, a)$	$Q_{\xi_1}(s, a)$ and $Q_{\xi_2}(s, a)$
Value	-	$V_{\zeta}(s)$ target $V_{\bar{\zeta}}(s)$
Actor	deterministic actor $\pi_{\phi}(s)$ target $\pi_{\bar{\phi}}(s)$	stochastic actor action sampled from conditional $\pi_{\phi}(a s)$
Reward	$r(s, a)$	$r(s, a) + \alpha \mathcal{H}(\pi(a s))$ $\mathcal{H}(\cdot)$ is the entropy reward is scaled by $1/\alpha$

Table 1. Comparison of the key features of TD3 and SAC.

The key step in Algorithm 1 is the learning step (line 11). Because our actions are continuous numbers, the RL agent works in continuous action spaces. There are several RL algorithms that we can use for this step, namely TD3 (Fujimoto et al. 2018) and SAC (Haarnoja et al. 2018). We give a brief overview of the inner workings of our RL agent, and for a more thorough overview, we refer the reader to (Silver et al. 2014; Lillicrap et al. 2015; Fujimoto et al. 2018; Haarnoja et al. 2018). The major components of the agent are:

- Actor: a deterministic actor with policy $\pi(s)$ will produce action a given the state s , $\pi(s) \rightarrow a$. In contrast, a stochastic actor will predict the conditional probability of an action, $\pi(a|s)$ given the state s . We can sample from this conditional distribution to get the action, $a \sim \pi(a|s)$.
- Critic: given the state s and taking the action a , the critic will evaluate the expected return q (a scalar), $Q(s, a) \rightarrow q$. The mapping $Q(\cdot, \cdot)$ is also called the state-action value function.
- Value: the value function $V(\cdot)$ will produce a scalar output given the state s , $V(s) \rightarrow v$. The value v gives a measure of the importance of the state s . In contrast to $Q(s, a)$, $V(s)$ is independent of the action taken at state s (but both follow the policy $\pi(\cdot)$).
- Replay buffer: the replay buffer stores the tuple (state s , action a , reward r , next state s') for each iteration t in Algorithm 1. This acts as a collection of past experience that helps the learning process.

Note that neither the actor, the critic nor the value function are dependent on past states, but only the current state and a measure of the state's favorability for future rewards, which is a characteristic of a Markov decision process (Sutton & Barto 2018). Looking into the future, the expected cumulative reward can be written as the Bellman equation

$$Q(s, a) = r + \gamma \max_{a'=\pi(s')} Q(s', a') \quad (15)$$

where s', a' is the (optimal) state action pair for the next step and $\gamma \approx 1$ is the discount factor for future uncertainty.

We model the actor, the critic and the value as deep neural networks with trainable parameters ϕ for the actor, ξ for the critic, and ζ for the value function. The use of these networks changes depending on the RL algorithm (TD3 or SAC). We list the main differences between TD3 and SAC in Table 1. In TD3, we train the actor and the critic as follows. Given the current state s , the actor tries to maximize $J(\phi) = Q(s, a)|_{a=\pi(s)}$ by choice of action. We perform gradient ascent on $J(\phi)$, with the gradient (using the chain rule) given as

$$\nabla_{\phi} J(\phi) = \nabla_a Q(s, a)|_{a=\pi(s)} \times \nabla_{\phi} \pi(s). \quad (16)$$

The critic is trained by minimizing the error between the current state-action value $Q(s, a)$ and the expected cumulative reward under

optimal settings (15)

$$J(\xi) = \|Q_{\xi}(s, a) - (r + \gamma \max_{a'=\pi(s')} Q(s', a'))\|^2. \quad (17)$$

In SAC, we train the value function by minimizing the cost

$$J(\zeta) = \|V_{\zeta}(s) - Q_{\xi}(s, a) + \log \pi_{\phi}(a|s)\|^2 \quad (18)$$

and thereafter, we train the state-action value function by minimizing

$$J(\xi) = \|Q_{\xi}(s, a) - (r + \gamma V_{\zeta}(s'))\|^2. \quad (19)$$

The SAC algorithm uses a stochastic policy, i.e., the actor gives the conditional probability of an action given the state. In order to train the actor, we sample from the posterior probability $\pi_{\phi}(a|s)$ and $\log \pi_{\phi}(a|s)$ is modeled as a mapping $f(\epsilon, s)$, with reparametrization noise ϵ (Kingma & Welling 2013). We perform gradient descent with the gradient

$$\begin{aligned} \nabla_{\phi} J(\phi) &= \nabla_{\phi} \log \pi_{\phi}(a|s) \\ &+ \nabla_a (\log \pi_{\phi}(a|s) - Q(s, a))|_{a=f(\epsilon, s)} \times \nabla_{\phi} f(\epsilon, s). \end{aligned} \quad (20)$$

In practice, RL is prone to instability and divergence, and therefore both TD3 and SAC use some of the following refinements (van Hasselt et al. 2015; Lillicrap et al. 2015; Fujimoto et al. 2018):

- Instead of having one critic, TD3 has two online ($Q_{\xi_1}(s, a)$ and $Q_{\xi_2}(s, a)$) and two target ($Q_{\bar{\xi}_1}(s', a')$ and $Q_{\bar{\xi}_2}(s', a')$) critics and selects the lower evaluation out of the two to evaluate (15). Similarly, SAC uses two online critics.
- TD3 uses both an online and a target actor. When evaluating (15), we use the target network to evaluate $\max_{a'=\pi(s')} Q(s', a')$.
- SAC uses both an online and a target value function. When evaluating (15), $\max_{a'=\pi(s')} Q(s', a')$ is replaced with $V_{\bar{\zeta}}(s)$.
- The parameters of the target networks are updated by a weighted average between the online and target parameters, and for the target actor in TD3, the update is only performed at delayed intervals.
- TD3 uses random actions at the start of learning for exploration, which is called the warmup period.
- Both TD3 and SAC keep a buffer to store past transitions: (s, a, r, s') that we re-use in mini-batch mode sampling during training (this is the replay buffer in Algorithm 1).

We refer the reader to Fujimoto et al. (2018) and Haarnoja et al. (2018) for detailed descriptions of TD3 and SAC. In section 4, we compare their performance in training our RL agent.

4 SIMULATIONS

As seen in Algorithm 1, we need simulations to train the RL agent. In contrast to conventional search-based methods in hyperparameter tuning (e.g., Bergstra & Bengio (2012); Bates et al. (2021)), the training phase of the RL agent needs additional computations. In a pipeline setting (Fig. 2), the tuning of hyperparameters needs to be done as fast as possible so that the flow of the data is not delayed. Therefore, after the training phase, our RL agent should run faster than conventional search-based methods. In section 4.1, to compare the performance of the RL agent with the performance of traditional grid search-based hyperparameter optimization, we consider an analogous but simpler pipeline than the calibration pipeline. We also compare the learning rates of DDPG, TD3 and SAC. Thereafter, in section 4.2, we describe the simulation setup to train the RL agent in calibration pipelines. We show the increase in reward (or score) of the RL agent as we

perform more simulations, hence confirming that the RL agent is able to learn.

4.1 Elastic net regression

In elastic net regression (Zou & Hastie 2005), we observe $\mathbf{x} \in \mathbb{R}^M$ given the design matrix $\mathbf{A} \in \mathbb{R}^{M \times M}$ and estimate the parameters $\boldsymbol{\theta} \in \mathbb{R}^M$ of the linear model $\mathbf{x} = \mathbf{A}\boldsymbol{\theta}$. The estimation is performed under regularization as

$$\hat{\boldsymbol{\theta}} = \arg \min_{\boldsymbol{\theta}} \left(\|\mathbf{x} - \mathbf{A}\boldsymbol{\theta}\|^2 + \rho_2 \|\boldsymbol{\theta}\|^2 + \rho_1 \|\boldsymbol{\theta}\|_1 \right) \quad (21)$$

where we have hyperparameters ρ_1 and ρ_2 . We can easily relate (21) to (8), which is our original problem. Moreover, (21) can also be considered as a simplified image deconvolution problem (see e.g., Ammanouil et al. (2019)), where \mathbf{x} is the visibility data, $\boldsymbol{\theta}$ is the image and \mathbf{A} is the de-gridding and Fourier transform operations (note that \mathbf{A} will not be a square matrix in this case).

Representing (21) as in (10) and using (14), for the elastic net problem, we have

$$\mathcal{A} = \mathbf{A} \frac{1}{2} \left(\mathbf{A}^T \mathbf{A} + (\rho_2 + \rho_1 \delta(\|\boldsymbol{\theta}\|)) \mathbf{I} \right)^{-1} \left(-2\mathbf{A}^T \right) \quad (22)$$

where $\delta(\cdot)$ is the Dirac delta function. We can use (22) to calculate the influence function. The RL agent for the elastic net regression hyperparameter selection interacts with its environment as follows:

- State: design matrix \mathbf{A} and eigenvalues $(1 + \lambda(\mathcal{A}))$.
- Action: regularization factors ρ_1, ρ_2 .
- Reward: $\frac{\|\mathbf{x}\|}{\|\mathbf{x} - \mathbf{A}\boldsymbol{\theta}\|} + \frac{\min(1 + \lambda(\mathcal{A}))}{\max(1 + \lambda(\mathcal{A}))}$.

Note that the reward considers both the (inverse) residual error as well as the bias (ratio of eigenvalues of the influence matrix). In this manner, we can achieve a balance between the bias and the variance of the residual.

For the simulations, we consider $M = 20$ and the agent is implemented in Pytorch (Paszke et al. 2017), within an *openai.gym* compatible environment². We use the limited-memory Broyden Fletcher Goldfarb Shanno (LBFGS) algorithm Yatawatta et al. (2019) to solve (21) and the Adam optimizer Kingma & Ba (2014) is used to train the agent.

The networks used for TD3 (and DDPG) RL agent are as follows. The critic uses two linear layers each for the state and for the action, finally combined in one linear layer to produce a scalar output. The actor uses four linear layers to produce the two dimensional output. We use exponential linear unit activation (Clevert et al. 2015) except in the last layer of the actor, where we use hyperbolic tangent activation (which is scaled to the valid range afterwards). We use batch normalization (Ioffe & Szegedy 2015) between all layers except the last. In the SAC RL agent, the actor produces two outputs, the mean and the standard deviation for the conditional probability of the action; apart from this the SAC actor is similar to the TD3 actor. The critic network is similar to the one in TD3. The value network is also similar to the critic, except that it only takes the state as input (no action is needed as input).

In each episode e in Algorithm 1, we create \mathbf{A} by filling its entries with unit variance, zero mean Gaussian random values. The ground truth value of the parameters, i.e. $\boldsymbol{\theta}_0$, is generated with the number of non-zero entries randomly generated in the range $[3, M]$ and these non-zero entries are filled with unit variance, zero mean Gaussian

random values. In order to get \mathbf{x} , we add unit variance, zero mean Gaussian noise to $\mathbf{A}\boldsymbol{\theta}_0$ with a signal to noise ratio of 0.1.

For each episode e , we limit the number of iterations to L . For TD3, we use a warmup interval of 100 iterations. In Fig. 3, we show the reward after each episode for different values of L . We have compared DDPG, TD3 and SAC algorithms in Fig. 3. We clearly see that both TD3 and SAC display stable learning after a certain number of episodes, unlike DDPG. We also see that SAC reaches a higher reward level, however at a lower rate than TD3.

As shown in Fig. 3, SAC RL agent reaches the highest reward level but TD3 achieves a stable reward earlier. We consider the TD3 RL agent, trained with $L = 4$ and $E = 1000$ using Algorithm 1, and compare its performance with traditional grid search based hyperparameter tuning. For the grid search, we use a grid of values $[0.001, 0.005, 0.01, 0.05, 0.1]$ for ρ_1 and ρ_2 . For the RL agent, we use $L = 4$ iterations to make a prediction for ρ_1 and ρ_2 while for the grid search we need at least $5 \times 5 = 25$ evaluations of (21). We compare the error ratio $\|\boldsymbol{\theta}_{RL} - \boldsymbol{\theta}_0\| / \|\boldsymbol{\theta}_{GR} - \boldsymbol{\theta}_0\|$ where $\boldsymbol{\theta}_0$ is the ground truth, $\boldsymbol{\theta}_{RL}$ is the solution obtained with hyperparameters determined by the RL agent and $\boldsymbol{\theta}_{GR}$ is the solution obtained with hyperparameters determined by grid search. We show histograms of this error ratio for 1000 episodes in Fig. 4.

As seen in Fig. 4, the trained RL agent is able to perform equally well as grid search, however the RL agent needs only 4 evaluation to make this prediction while grid search uses 25 evaluations. This makes a strong case for using RL for hyperparameter tuning, especially in a situation where data is processed in a pipeline.

4.2 Calibration

We give a summary of the calibration pipeline, i.e. the environment in Fig. 2. The observation consists of $N = 62$ stations. The data passed through the calibration pipeline have 1 sec integration time and 8 frequencies in the range $[115, 185]$ MHz. Calibration is performed for every $\Delta_t = 10$ time samples (every 10 sec, $D = 151\ 280$) and 6 such calibrations are performed to interact with the RL agent. In other words, 1 min of data are used by the agent to make a recommendation on the regularization parameters. In practice, the first 1 min of data is used to adjust the hyperparameters of the pipeline, and thereafter, the pipeline is run unchanged for the full observation (which typically will last a few hours). We use SAGECal³ for calibration and excon⁴ for imaging.

We simulate data for calibration along $K = 4$ directions in the sky, with systematic errors \mathbf{J}_{kpf} in (1) that are smooth both in time and in frequency, but have random initial values. One direction out of K represents the observed field, and its location is randomly chosen within 1 deg radius from the field centre. The remaining $K - 1$ directions play the role of outlier sources (for instance sources such as the Sun, Cassiopeia A, Cygnus A) and are randomly located within a 15 deg radius from the field centre. The intensity of the central source is randomly selected within $[3, 10]$ Jy. The intrinsic intensities of the outlier sources are randomly selected within $[100, 250]$ Jy. An additional 200 weak sources (point sources and Gaussians) with intensities in $[0.01, 0.1]$ Jy (power law distribution with exponent -2) are randomly positioned across a 16×16 square degrees surrounding the field centre. The spectral indices of the K sources being calibrated are generated from a standard normal distribution and all the weak sources have flat spectra. The simulation includes

² <https://gym.openai.com/>

³ <http://sagecal.sourceforge.net/>

⁴ <https://sourceforge.net/projects/exconimager/>

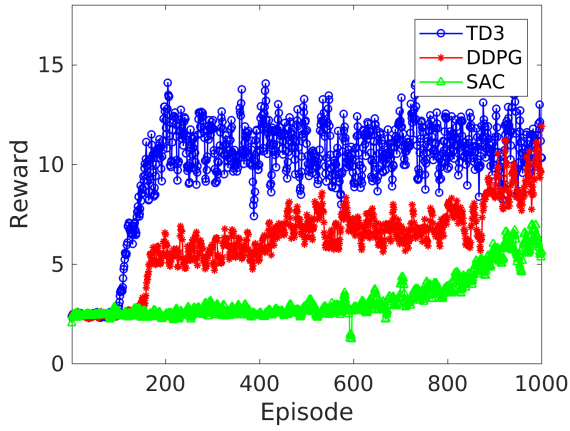
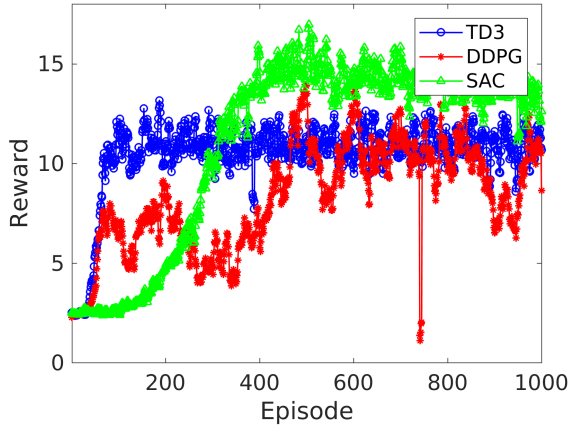
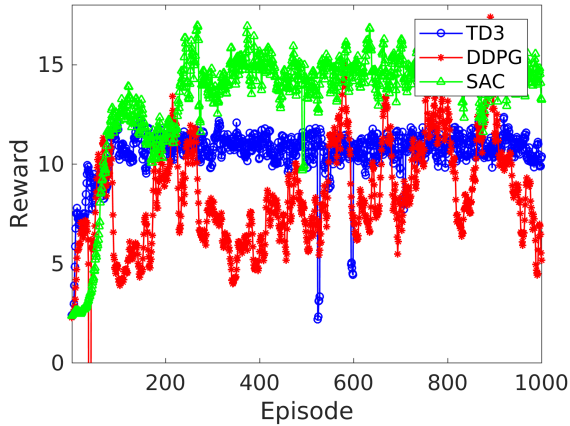
(a) $L = 1$ (b) $L = 4$ (c) $L = 20$

Figure 3. The score variation with episode for the agent selecting hyperparameters in elastic net regression. The number of iterations for each episode L is varied from (a) $L = 1$ (b) $L = 4$ and (c) $L = 20$. We see that TD3 algorithm learns faster, but SAC reaches a higher reward for large number of episodes.

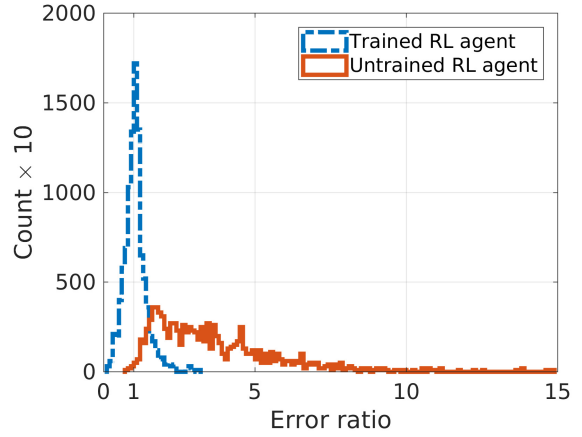


Figure 4. Histogram comparison of the error ratio for hyperparameter tuning using grid search against using TD3 RL agent. Results using both the untrained and trained RL agent are shown. With the trained RL agent, we get a mean result of about 1 indicating that the RL agent is able to predict as equally well as using grid search.

the effect due to the station beam shape. Finally, zero mean, complex circular symmetric Gaussian noise is added to the simulated data with a signal to noise ratio of 0.05. Note that the sky model used for calibration only includes the K sources (not the weak sources) and the $K - 1$ outlier sources have their intensities divided by a factor of 100 to account for the receiver beam attenuation (apparent value).

The RL agent used in the calibration pipeline interacts with the environment (or the pipeline) as follows:

- State: the sky model used in calibration and the influence map $\mathcal{I}(\theta)$ generated using 1 min of data.
- Action: regularization factors ρ_k for K directions.
- Reward: $\frac{\sigma_0}{\sigma_1} + \frac{1}{\sigma(\mathcal{I}(\theta))}$, where σ_0 and σ_1 are the image noise standard deviations of the input data and output residual, respectively. The standard deviation of $\mathcal{I}(\theta)$ is given by $\sigma(\mathcal{I}(\theta))$.

In Fig. 5, we show the residual image standard deviation, influence map standard deviation and the calculated reward. The x -axis corresponds to the regularization parameters ρ_k , scaled up and down by factors of ten (starting from the regularization that gives the highest reward). For low regularization values, we see more or less constant residual image noise, however, we clearly see a high level of influence. This high influence on the left hand side of Fig. 5 implies high variance of θ (due to the unmodeled sources in the sky) and as a consequence, we should expect high level of weak signal suppression. On the other hand, on the right hand side of Fig. 5, for high regularization, we see increased residual image noise, meaning poor calibration. We compose our reward to reach a balance between the bias and variance of the residual.

We use both TD3 and SAC for training our RL agent. The RL agents and the environment are quite similar to the ones used in elastic net regression. In TD3, the critic uses 3 convolutional layers to process the influence map, and two linear layers to process the action and the sky model. These two are combined at the final linear layer. The actor also uses 3 convolutional layers to process the influence map and two linear layers for the sky model. Once again, they are combined at the final linear layer. The first three layers of both the actor and critic use batch normalization. The activation functions are exponential linear units except at the last layer of the actor, where we

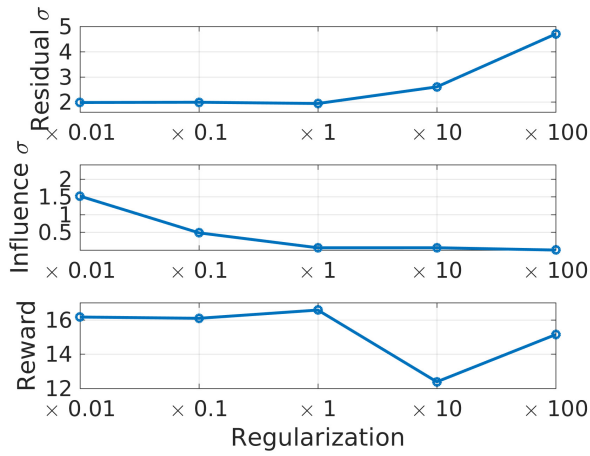


Figure 5. The residual noise, the influence map noise and the reward for various values of regularization. The regularization factors are scaled up and down from the optimal values ($\times 1$).

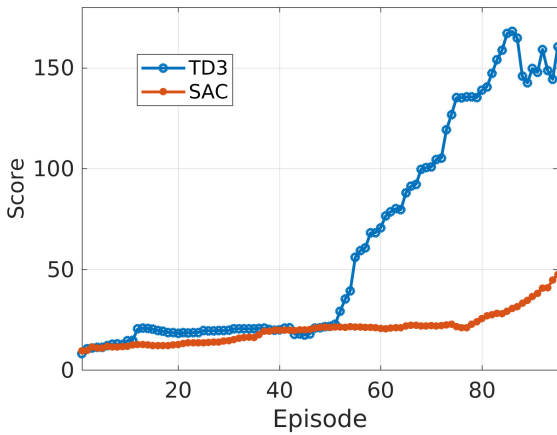


Figure 6. The variation of the score (or the reward) with episode for the TD3 and SAC RL agents in calibration. The number of iterations for each episode is $L = 4$. The TD3 RL agent is able to reach a higher score much faster than the SAC RL agent.

use hyperbolic tangent activation. The action is scaled to the required range by the environment. In the SAC RL agent, the critic is similar to the one in the TD3 RL agent. The actor is almost the same, except it produces two outputs, for the mean and the standard distribution of the conditional probability of the action. The value network is similar to the critic, except it does not process the action as an input.

The training of our RL agents are done as in Algorithm 1. In each episode e , we generate a random sky model and data as described previously. The pipeline is run with initial regularization factors determined analytically (Yatawatta 2016). The state information generated by the pipeline is fed into the RL agent to retrieve updated regularization factors. The pipeline is run again and we repeat the cycle. Using the results shown in Fig. 3, we limit the number of such iterations per each episode to $L = 4$. At the final iteration, we record the reward (or the score) to measure the progress of the agent. The score variation over a number of such episodes is shown in Fig. 6.

After about 50 episodes, we see the TD3 RL agent reaching a

higher score (the average reward at each episode) in Fig. 6, indicating that the agent is able to learn and improve its recommendations for the regularization factors to use. The SAC RL agent is learning at a lower rate, and this behavior is similar to the elastic net regression RL agent, as seen in Fig. 3 (b). Once we have a fully trained agent, following Algorithm 1, we omit the simulation step (line 4). The state is determined using 1 min of data and we use $L = 4$ iterations to make a recommendation for the hyperparameters. We will get a result similar to Fig. 1 bottom row with the recommendation. We can keep the pipeline running with the same hyperparameters for a much longer time or dynamically adjust the hyperparameters of the pipeline by interacting with the RL agent. This aspect needs more work with real data, which we intend to pursue as future work. In addition, we can develop similar agents for other data processing steps in radio astronomy, including RFI mitigation and image synthesis. Extending beyond radio astronomy, similar techniques can be applied in other data processing pipelines in general machine learning problems.

5 CONCLUSIONS

We have introduced the use of reinforcement learning in hyperparameter tuning of radio astronomical calibration pipelines. By using both the input-output noise reduction as well as the influence function to determine the reward offered to the RL agent, we can reach a balance between the bias and the variance introduced by the pipeline. As illustrated by the elastic-net regression example, we can also apply the same technique to many other data processing steps, not only in radio astronomy but also in other applications.

ACKNOWLEDGMENTS

We thank the anonymous reviewer for the careful review and valuable comments.

DATA AVAILABILITY

Ready to use software based on this work and test data are already available online⁵.

REFERENCES

- Ammanouil R., Ferrari A., Mary D., Ferrari C., Loi F., 2019, Monthly Notices of the Royal Astronomical Society, 490, 37
- Bates S., Hastie T., Tibshirani R., 2021, arXiv e-prints, p. [arXiv:2104.00673](https://arxiv.org/abs/2104.00673)
- Bergstra J., Bengio Y., 2012, Journal of Machine Learning Research, 13, 281
- Boyd S., Parikh N., Chu E., Peleato B., Eckstein J., 2011, Foundations and Trends® in Machine Learning, 3, 1
- Brossard M., El Korso M. N., Pesavento M., Boyer R., Larzabal P., Wijnholds S. J., 2016, preprint, ([arXiv:1609.02448](https://arxiv.org/abs/1609.02448))
- Clevert D.-A., Unterthiner T., Hochreiter S., 2015, arXiv e-prints,
- Cook R., Weisberg S., 1982, Residuals and Influence in Regression. Monographs on statistics and applied probability, Chapman & Hall, [http://books.google.nl/books?id=MVSqAAAAIAAJ](https://books.google.nl/books?id=MVSqAAAAIAAJ)
- Fujimoto S., van Hoof H., Meger D., 2018, arXiv e-prints, p. [arXiv:1802.09477](https://arxiv.org/abs/1802.09477)
- Geman S., Bienenstock E., Doursat R., 1992, *Neural Computation*, 4, 1
- Haarnoja T., Zhou A., Abbeel P., Levine S., 2018, arXiv e-prints, p. [arXiv:1801.01290](https://arxiv.org/abs/1801.01290)

⁵ <https://github.com/SarodYatawatta/smart-calibration>

- Hamaker J. P., Bregman J. D., Sault R. J., 1996, *Astronomy and Astrophysics Supp.*, 117, 137
- Hampel F. R., Ronchetti E., Rousseeuw P. J., Stahel W. A., 1986, *Robust statistics: the approach based on influence functions*. New York USA: Wiley, <https://archive-ouverte.unige.ch/unige:23238>
- Hestenes M. R., 1969, *Journal of Optimization Theory and Applications*, 4, 303
- Ioffe S., Szegedy C., 2015, arXiv e-prints, [p. arXiv:1502.03167](https://arxiv.org/abs/1502.03167)
- Kingma D. P., Ba J., 2014, preprint, ([arXiv:1412.6980](https://arxiv.org/abs/1412.6980))
- Kingma D. P., Welling M., 2013, arXiv e-prints, [p. arXiv:1312.6114](https://arxiv.org/abs/1312.6114)
- Koh P. W., Liang P., 2017, in Precup D., Teh Y. W., eds, *Proceedings of Machine Learning Research Vol. 70*, *Proceedings of the 34th International Conference on Machine Learning*. PMLR, International Convention Centre, Sydney, Australia, pp 1885–1894, <http://proceedings.mlr.press/v70/koh17a.html>
- LeCun Y., Bengio Y., Hinton G., 2015, *Nature*, 521, 436 EP
- Lillicrap T. P., Hunt J. J., Pritzel A., Heess N., Erez T., Tassa Y., Silver D., Wierstra D., 2015, arXiv e-prints, [p. arXiv:1509.02971](https://arxiv.org/abs/1509.02971)
- McMahan B. H., Moore E., Ramage D., Hampson S., Agüera y Arcas B., 2016, arXiv e-prints, [p. arXiv:1602.05629](https://arxiv.org/abs/1602.05629)
- Mertens F., et al., 2020, *Monthly Notices of the Royal Astronomical Society*, 493, 1662
- Mevius M., et al., 2021, pre-print
- Mnih V., et al., 2015, *Nature*, 518, 529
- Ollier V., Korso M. N. E., Ferrari A., Boyer R., Larzabal P., 2018, *Signal Processing*, 153, 348
- Paszke A., et al., 2017, in NIPS-W.
- Patil A. H., et al., 2017, *ApJ*, 838, 65
- Powell M., 1969, *Optimization*, pp 283–298
- Silver D., Lever G., Heess N., Degris T., Wierstra D., Riedmiller M., 2014, in *Proceedings of the 31st International Conference on International Conference on Machine Learning - Volume 32*. ICML 2014. JMLR.org, pp 387–395
- Sutton R. S., Barto A. G., 2018, *Reinforcement Learning: An Introduction*. A Bradford Book, Cambridge, MA, USA
- Thompson A., Moran J., Swenson G., 2001, *Interferometry and synthesis in radio astronomy* (3rd ed.). Wiley Interscience, New York
- Yatawatta S., 2015, *MNRAS*, 449, 4506
- Yatawatta S., 2016, in *24th European Signal Processing Conference (EU-SIPCO)*, 2016.
- Yatawatta S., 2018, in *2018 IEEE 10th Sensor Array and Multichannel Signal Processing Workshop (SAM)*. pp 485–489, [doi:10.1109/SAM.2018.8448481](https://doi.org/10.1109/SAM.2018.8448481)
- Yatawatta S., 2019, *Monthly Notices of the Royal Astronomical Society*, 486, 5646
- Yatawatta S., 2020, *Monthly Notices of the Royal Astronomical Society*, 493, 6071
- Yatawatta S., Diblen F., Spreeuw H., Koopmans L. V. E., 2018, *MNRAS*, 475, 708
- Yatawatta S., De Clercq L., Spreeuw H., Diblen F., 2019, in *2019 IEEE Data Science Workshop (DSW)*. pp 208–212, [doi:10.1109/DSW.2019.8755567](https://doi.org/10.1109/DSW.2019.8755567)
- Zou H., Hastie T., 2005, *Journal of the Royal Statistical Society: Series B (Statistical Methodology)*, 67, 301
- van Hasselt H., Guez A., Silver D., 2015, arXiv e-prints, [p. arXiv:1509.06461](https://arxiv.org/abs/1509.06461)

This paper has been typeset from a $\text{\TeX}/\text{\LaTeX}$ file prepared by the author.